Troposphere Sensing Using Grazing-Angle GNSS-R Measurement from LEO Satellites

Yang Wang[1]

[1]University of Colorado Boulder

November 28, 2023

Troposphere Sensing Using Grazing-Angle GNSS-R Measurement from LEO Satellites

Yang Wang

Ann & H. J. Smead Aerospace Engineering Sciences Department, University of Colorado Boulder, Boulder, Colorado, USA.

Key Points:

- A new tropospheric sensing concept is studied that relies on coherent-reflection GNSS signals off ocean and ice surfaces.
- Algorithms are developed and demonstrated using Spire grazing-angle GNSS-R data to retrieve tropospheric delay and water vapor.
- The presented approach provides high-precision tropospheric delay and TCWV horizontal profiles, as validated using the Sentinel-3 OLCI data.

Corresponding author: Yang Wang, `yang.wang-2@colorado.edu`

Abstract

This paper studies a new concept of using GNSS signals coherently reflected over relatively smooth ocean and ice surfaces from very low elevation angles (below ∼8°) and received by low Earth orbit (LEO) satellites to retrieve the tropospheric information. This approach can provide horizontal profiles of tropospheric zenith delay and total column water vapor (TCWV) with centimeter-level high precision and spatial resolutions of 10s of km by ∼1 km, depending on the elevation angle, with a sampling spacing of ∼100 m. This approach can potentially be applied to most sea ice and calm ocean areas and provide tropospheric sensing data, which can complement and augment existing observation systems. A few case studies are conducted in this paper using the Spire grazing-angle GNSS-R data. The retrieved TCWV is compared to ERA5 products and the Sentinal-3 OLCI measurements and shows promising performances. The errors associated with the GNSS-R tropospheric measurements are also discussed.

Plain Language Summary

The atmospheric water vapor is an important component for the weather and climate systems and is difficult to measure, especially over ocean and ice surfaces. This paper studies a new approach to measuring atmospheric water vapor using global navigation satellite system (GNSS) signals reflected off ocean and ice surfaces. If the reflection is from a low elevation angle (below ∼8°) and the reflected signal is coherent (all signal rays are reflected in the same direction), this approach can provide very high precision observation of the horizontal gradients of the tropospheric delay and the vertically integrated atmospheric water vapor with good spatial resolutions. This paper presents the methodology of the proposed approach and a few case studies to demonstrate the feasibility and performance by comparing the GNSS-R retrieved water vapor measurements with models and the Sentinel-3 satellite radiometry measurements. The errors associated with the GNSS Reflectometry (GNSS-R) tropospheric measurements are also discussed.

1 Introduction

Atmospheric water vapor is a dynamic and influential component of Earth's climate and weather systems. As the most abundant greenhouse gas, water vapor is of great importance to the Earth's radiative balance, and it also plays a crucial role in the global atmospheric circulation, water cycle, and thus climate changes (Schneider et al., 2010). On smaller spatio-temporal scales, the water vapor content affects local weather conditions and regional water cycles (Bengtsson & Hodges, 2005; Sherwood et al., 2010), and the movement of water vapor is important for determining the amount of precipitation a region receives. Global atmospheric water vapor has very likely been increasing due to global warming since the 1980s as reported by The Sixth Assessment Report of the United Nations (UN) Intergovernmental Panel on Climate Change (IPCC) (Masson-Delmotte et al., 2021). It thus tends to aggravate various extreme weather and climate events, such as floods and droughts (Turato et al., 2004; Ault, 2020). Therefore, the analysis of atmospheric water vapor is essential for deepening our understanding of the Earth system and improving the capabilities of climate and weather forecasts.

Total column water vapor (TCWV), also referred to as integrated water vapor (IWV) or total precipitable water (TPW), is a measure of the total gaseous water contained in a vertical column of atmosphere and one of the essential climate variables defined by the GCOS (Global Climate Observing System) Climate Monitoring Principles (Bojinski et al., 2014). Because of its importance in weather and climate modeling and prediction, TCWV has been continuously observed for decades using a wide range of methods, including ground-based, in-situ, and remote sensing techniques such as radiosonde, radiometry, Lidar, Very Long Baseline Interferometry (VLBI), ground-based GNSS receiver networks, GNSS radio occultation (RO), etc. (Z. Li et al., 2003; Miloshevich et al., 2006; Niell et al., 2001;

Elgered et al., 1991; Ismail & Browell, 1989; Bevis et al., 1992; Anthes, 2011; Kuo et al., 2000). However, there is still a demand for accurate TCWV observation, especially over the ocean and polar ice, due to the challenges in deploying ground-based and airborne sensors in inaccessible areas or harsh environments and the various limitations associated with these above-mentioned techniques. Satellite observation using passive imagers is a primary remote-sensing data source of TCWV over the ocean. A polar-orbiting satellite can provide daily and almost global coverage, but this approach is associated with high costs and also has limitations in accuracy and availability. For example, the Ocean and Land Color Instrument (OLCI) onboard Sentinel-3 satellites have large biases and variations over water (9.24 kg/m^2 mean bias and 12.3 kg/m^2 RMSD for Sentinel-3A and similar performance for Sentinel-3B), according to the Sentinel-3 Optical Annual Performance Report in 2022, and it cannot provide observation with cloud coverage and has poor performance over ice. As analyzed by Yuan et al. (2023), a GNSS network-based IWV dataset has biases within $\pm$ 3.0 kg/m^2 with a mean absolute bias value of 0.69 kg/m^2, and the standard deviations are no larger than 3.4 kg/m^2. This demonstrates the GNSS signal being a viable source for accurate TCWV observation, though the ground GNSS networks have limited spatial coverage. GNSS RO provides global observation of vertical atmospheric profiles but also has its own limitations, i.e., the poor horizontal resolution, potential retrieval errors due to significant refractivity gradients, and the RO signal cannot always probe deep into the troposphere bottom (Steiner & Kirchengast, 2005).

GNSS signals can be coherently reflected from the calm ocean and relatively smooth ice surfaces and offer cm-level high precision ranging measurements. Such measurements have been demonstrated for precise surface height retrieval, such as sea level anomaly (SLA) and sea ice freeboard (W. Li et al., 2017; Cardellach et al., 2019; Nguyen et al., 2020; Wang et al., 2020; Wang & Morton, 2021a). The tropospheric delay may cause significant errors in GNSS-R altimetry retrieval, especially at low elevation angles, however, the amplification of troposphere delay errors by low elevation angles offers an opportunity to retrieve the tropospheric delay and water vapor content. This paper demonstrates a new approach to retrieving tropospheric delay and TCWV from grazing-angle GNSS reflectometry (GNSS-R) using data from Spire CubeSats. Grazing-angle GNSS-R can potentially fill some of the atmospheric water vapor observation data gaps and provide complementary observations over the ocean and polar ice with high accuracy, high spatial and temporal resolutions, and low cost compared with other satellite observation techniques.

2 Troposphere Sensing Using Grazing-Angle GNSS-R

GNSS-R utilizes signals reflected from the Earth's surface and received by a downward-looking antenna onboard a low Earth orbiting (LEO) satellite to sense the reflection surface and signal propagation environment (e.g., ionosphere and troposphere) properties. Recent research has shown that GNSS signals reflected over sea ice and calm waters and received by low-cost LEO small satellites contain sufficient coherent energy to be processed to achieve centimeter-level ranging precision. In a series of case studies using Spire CubeSats data and raw data samples from TechDemoSat-1 and Cyclone GNSS (CYGNSS) satellites, GNSS-R phase altimetry is reported to have the capability to achieve 10 cm or better precision in relative surface height retrieval over ice, calm ocean, lakes, and rivers (W. Li et al., 2017, 2018; Cardellach et al., 2019; Nguyen et al., 2020; Wang et al., 2020; Wang & Morton, 2021c; Roesler et al., 2021). However, it is also recognized that the tropospheric delay is a significant error source to GNSS-R phase altimetry at grazing angles, though there is a need for more thorough evaluations and characterizations.

A low elevation angle affects oppositely the retrievals of surface elevation and tropospheric delay in GNSS-R. For example, a 1-cm troposphere zenith delay deviation is amplified to $\sim$68.5 cm in the surface height retrieval at 5° elevation angle (Wang et al., 2020), and conversely, a sub-meter surface elevation deviation (larger than the sea level model errors in most occasions) causes minor errors in the tropospheric delay retrieval at 5°. It should be noted that the GNSS-R carrier phase can only provide relative measurements for both reflection surface height and tropospheric delays. Since the troposphere model error is mainly due to uncertainty in the wet delay, this amplification of tropospheric error in GNSS-R at low elevation angles offers an opportunity to retrieve the water vapor content, e.g., the TCWV horizontal gradient, if the reflection surface height variations are well modeled. The sea and sea ice surface elevations can be modeled using the mean sea surface (MSS), ocean tide models, and sea level anomaly or ice freeboard data products. Coherent GNSS signal reflections are also available over some of the Antarctic areas (Wang, 2023), however, the surface elevation is more complicated, thus the feasibility, the uncertainties of the elevation models, and other error sources in tropospheric retrievals need to be further evaluated but are out of the scope of this paper.

The grazing-angle GNSS-R observation of the troposphere as proposed in this paper is illustrated below in Figure 1. The desired range of elevation angle for the tropospheric retrieval is below ~8°. This paper focuses on the GNSS-R signals with elevation angles from 3° to 8° (a rough estimate and to be optimized for different regions). The main reasons for this elevation angle range are that: 1) below ~8°, the surface elevation variations tend to have minor impacts; 2) the tropospheric mapping functions, such as the Vienna Mapping Function 3 (VMF3) (Landskron & Böhm, 2018), usually have a cut-off elevation angle of ~3° or higher; with an empirical mapping function, the GNSS-R derived slant tropospheric delays can be easily converted into zenith delays, under certain assumptions, and this enables a quick validation of the proposed approach using TCWV models or other sensor measurements. Below 3° elevation angle, the GNSS-R signals are still excellent sources for tropospheric sensing, but the atmospheric bending effects tend to be more dominant in the observed GNSS-R excess range, thus the water vapor retrieval will be based on bending models and is not studied in this paper.

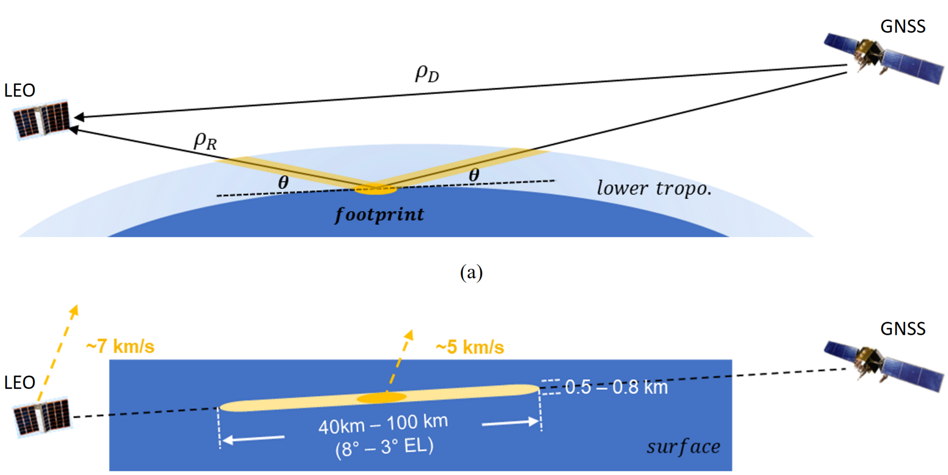

Figure 1: Illustration of spaceborne grazing-angle GNSS-R and its application in tropospheric sensing. (a) Reflection plane; (b) Projection onto reflection surface. EL: elevation angle at the specular point (center of the reflection footprint). The black dashed line is the same as in Figure 1(a) and projected onto the reflection surface.

At 3° to 8° elevation angles, as shown in Figure 1, the GNSS-R signal reflection has an elliptical footprint (approximated by the first Fresnel zone) with a size of a few kilometers by 0.5-0.8 km. The signal propagates through 40-100 km horizontal distances in the lower troposphere (below 3 km) with high water vapor concentration, and as the LEO satellite moves very fast at ∼7.8 km/s, it drives the reflection "footprint" and the signal propagating in the troposphere to also move at high speeds, around 5 km/s, and scan through the troposphere. The 50-Hz rate of Spire data corresponds to 100-m spacing of troposphere sampling. The GNSS-R signals can thus offer horizontal profiles of the tropospheric delay and TCWV with a spatial resolution of about 40-100 km by ∼1 km, as shown in Figure 1(b), and a high sampling rate of ∼100 m, and the reflection footprint could move towards any direction depending on the relative motion between the LEO and GNSS satellites. The carrier phase-based measurement has a high precision of centimeters or even sub-centimeter, however, it can only measure the gradients of slant tropospheric delays due to unresolved phase ambiguities.

3 Data and Methodology

3.1 Spire Grazing-Angle GNSS-R Data and Processing

The grazing-angle GNSS-R data used in this study is obtained from Spire Global Inc.'s CubeSats, which were originally designed for GNSS RO and later adjusted to also operate GNSS-R data collection for sea ice extent and ocean altimetry applications (Jales et al., 2020). The data was made available through NASA's Commercial Smallsat Data Acquisition (CSDA) Program. Orbiting the Earth at 480-600 km altitudes, these CubeSats are equipped with a zenith antenna for precise orbit determination (POD) and forward- or backward-looking right-hand circular polarization (RHCP) antennas to collect RO and direct and reflected GNSS signals. Spire's LEMUR-2 GNSS receivers perform open-loop tracking of dual-frequency and multi-constellation GNSS signals and generate 50-Hz I/Q (In-phase/Quadrature) correlator outputs, along with providing 1-Hz POD data. The Spire CubeSats have been conducting grazing-angle GNSS-R data primarily in high latitudes and selected low-latitude ocean regions, with an elevation angle (at the SP) range of 5° to 30°. Very occasionally, lower elevation angle (0-5°) GNSS-R data is also found collected, such as the example shown in Figure 2.

The Spire's LEMUR-2 GNSS receivers collect GNSS-R or RO data (conduct correlations between received and locally generated reference signals) regardless if the signal contains sufficient coherent energy. Even for GNSS-R signals classified as coherent reflections, the phase measurements usually have relatively low signal-to-noise ratio (SNR) and coherence levels, which result in large phase noise and cycle slips. The processing of Spire grazing-angle GNSS-R data consists of mainly two stages, i.e., coherence detection and phase reconstruction. The GNSS-R phase coherence can be quantified based on the phase noise statistics, e.g., circular length and kurtosis (Roesler et al., 2021), SNR, and other metrics (Loria et al., 2023). This paper used the circular length ζ of phase difference $\dot{\delta\phi}$, $\dot{\delta\phi}[k] = \delta\phi[k+1] - \delta\phi[k]$, over 1 second (50 samples) for coherence detection:

$$\zeta = \frac{1}{N}\left|\sum_{i=1}^{N} \cos\dot{\delta\phi}_i + \sum_{i=1}^{N} \sin\dot{\delta\phi}_i\right| \tag{1}$$

where ζ is calculated for a set of $\dot{\delta\phi}_i$, with $i = 1, 2, 3, ..., N$, and $\delta\phi$ is the measurement of residual phase as obtained from the I/Q correlation outputs, i.e., $\delta\phi = atan2(Q, I)$, with the navigation data bits wiped off from I/Q. ζ has values in a range of $[0, 1]$, and it is closer to 1 if the signal is more coherent. The phase reconstruction (mainly cycle-slip correction) is performed by the Simultaneous Cycle-slip And Noise Filtering (SCANF) method developed by Wang et al. (2020). The cycle-slip correction is important to this application as the example shows in Figure 2e. The Spire phase data circular length (calculated for 1-sec phase difference) is found to usually have a noise floor below ∼0.25, such as in Figure 2d, latitude range 42°-44° N, where the reflection is off land surface. Heuristically, $\zeta_{L1} + \zeta_{L2} > 0.8$ is found to be an appropriate threshold that most Spire grazing-angle reflection GPS phase data meeting this criterion has sufficient reflection coherence and can be processed for altimetric retrievals with SCANF.

3.2 Tropospheric Delay and TCWV Retrievals

The retrieval of tropospheric information from spaceborne GNSS-R follows the reflected signal phase-range model and measurement equations below (similar to phase altimetry):

$$\begin{aligned}\Phi_R(t) =& |\mathbf{r}_{\mathrm{tx}}(t-\Delta t_R)-\mathbf{r}_{\mathrm{sp}}(t)|+|\mathbf{r}_{\mathrm{sp}}(t)-\mathbf{r}_{\mathrm{rx}}(t)|+I_R(t)+T_R(t)\\ &+b_{\mathrm{tx}}(t-\Delta t_R)-b_{\mathrm{rx}}(t)\end{aligned} \tag{2}$$

$$\hat{\Phi}_R(t)=\tilde{\Phi}_R^{OL}(t)+\delta\hat{\Phi}_R(t)+N(t)\lambda+n(t) \tag{3}$$

where Φ represents the phase range in the unit of meter, subscript R denotes the reflected signal, Φ_R is the reflected signal phase range, $\tilde{\Phi}_R^{OL}$ is the reflected phase-range model used in the onboard open loop tracking, $\delta\hat{\Phi}_R$ is the residual phase range measurement from open loop tracking output, $\mathbf{r}$ with subscripts denotes the position vector of GNSS satellite, specular point, and LEO satellite, respectively, in an Earth-centered Earth-fixed (ECEF) coordinate, I is the ionospheric phase advance, T is the tropospheric delay, N is an unknown integer number representing the phase ambiguity, λ is the signal wavelength, e.g., $\lambda_{L1}=19.03\ cm$ for GPS L1 signal, and n is the phase measurement noise.

Here we assume a well-modeled surface elevation. For example, for reflection over the ocean, the ocean surface height is modeled as a summation of the DTU21 MSS (Andersen et al., 2023), TPXO 8 global ocean tide model (Egbert & Erofeeva, 2002), and the SLA grid data. The precise GNSS and LEO satellite orbits and clock biases are obtained from CODE (Center for Orbit Determination in Europe) final orbit and Spire POD data products respectively, then based on the precise orbits and the surface elevation models the specular point $\mathbf{r}_{\mathrm{sp}}$ is estimated in the Spire data processing. The relative ionosphere effects (with unresolved phase ambiguities) on the reflected signal phase are estimated using dual-frequency measurements. As a result, we can estimate the GNSS-R slant tropospheric delay:

$$\hat{T}_R(t)=\hat{\Phi}_R(t)-\hat{g}_R(t)-\hat{I_R}(t)+M(t)\lambda+\epsilon(t) \tag{4}$$

where $\wedge$ denotes the estimation of variables in Eq. (2) and g_R, g_R represents the geometric and clock components in Eq. (2), M is another unknown integer number representing the phase ambiguity, ϵ represents the impacts from various estimation errors and noise. The slant tropospheric delay can be modeled as:

$$T_R(t)=2\times(ZHD(t)\times m_{dry}(\theta(t))+ZWD(t)\times m_{wet}(\theta(t))) \tag{5}$$

where m_{dry} and m_{wet} are the mapping functions for the zenith hydrostatic delay (ZHD) and zenith wet delay (ZWD), respectively. This paper uses the VMF3 (Landskron & Böhm, 2018) mapping functions and the associated $1°\times1°$ grid data of ZHD and ZWD. Assuming the ZHD is stable and well modeled, the ZWD estimation based on Eq. (4, 5) is derived as:

$$\widehat{ZWD}(t)=\frac{\frac{1}{2}\hat{T}_R(\theta(t))-\widetilde{ZHD}(t)\times m_{dry}(\theta(t))-M(t)\lambda}{m_{wet}(\theta(t))} \tag{6}$$

where $\widetilde{ZHD}$ is interpolated from the grid data and M, again, is an unknown integer number representing the unsolvable phase ambiguity. Therefore, an assumption has to be made, e.g., the mean ZWD over the GNSS-R track area (usually a few to several hundreds of kilometers) is accurate, then GNSS-R provides a high precision estimation of the ZWD horizontal profile, which has a mean value that is very close to the interpolated $\widetilde{ZWD}$ from the grid data:

$$\delta\hat{T}_R(t)=\frac{1}{2}\hat{T}_R(\theta(t))-\widetilde{ZHD}(t)\times m_{dry}(\theta(t))-\widetilde{ZWD}(t)\times m_{wet}(\theta(t)) \tag{7}$$

$$\widehat{ZWD}(t) = \frac{\delta\hat{T}_R(t) - \overline{\delta\hat{T}_R}}{m_{wet}(\theta(t))} + \widetilde{ZWD}(t) \quad (8)$$

where $^{-}$ denotes the mean value of a time sequence. The ZWD estimates are then converted into TCWV using the following equations:

$$TCWV = \Pi \times ZWD \quad (9)$$

$$\Pi = \frac{10^6}{R_V \cdot (k_2' + k_3/T_m)} \quad (10)$$

where Π is the conversion factor in the unit of kg$\cdot$m$^{-2}\cdot$mm^{-1}, $R_V = 461.522$ J$\cdot$kg$^{-1}\cdot$ K^{-1} is the specific gas constant for water vapor, $k_2' = 22.1$ K$\cdot$hPa^{-1} and $k_3 = 373900$ K$^2\cdot$ hPa^{-1} are the atmospheric refractivity constants, and T_m is the weighted mean atmosphere temperature (Bevis et al., 1992, 1994). Yuan et al. (2023) used the ECMWF Reanalysis v5 (ERA5) pressure level products (with 37 vertical pressure levels) to estimate T_m, and this paper used a simpler approximation of T_m following Alshawaf et al. (2015):

$$T_m = 70.2 + 0.72T_s \quad (11)$$

where T_s is the surface temperature (using the 2-meter temperature from the ERA5 single level products).

4 Results

This section presents case studies to validate the feasibility and show the performance of the proposed approach. The first example as shown in Figure 2 used a Spire grazing-angle GNSS-R dataset of dual-frequency (L1&L2) GPS signals reflected over the ocean from $\sim$0$-$8° elevation angles. The pink/red tracks in Figure 2a-c are the GNSS-R SP track, with the latitude range shown in the x-axis in Figure 2d-f. The pink segment (Lat: 41.6°-44°) is of reflections mostly over the land surface and appears to be dominantly non-coherent scattering. Figure 2a shows the map of the horizontal wind at 10-m altitude using data from ERA5 single level products, which is also interpolated for the SP track and shown in Figure 2e (corresponding to the right y-axis). Figure 2b is a similar plot showing the map of the significant ocean wave heights due to wind waves (using data from ERA5). Figure 2d shows the L1&L2 SNR and phase circular length estimates, see Eq. (1), both at 1-Hz and can be used as metrics representing the signal reflection coherence. The land-reflection (pink) segment shows the "noise floors" of both metrics, and the rest of the signal reflected over the ocean shows at least some detectable coherence energy. The signal in the latitude range of 44°-55° has sufficient coherence energy, based on the suggested criterion $\zeta_{L1} + \zeta_{L2} > 0.8$, and the signal at latitudes >55° seems to also provide effective measurements in this example. Figure 2e, left y-axis, shows the residual phase measurement (containing mainly the ionosphere effects, mismodeled tropopsheric delay, and noise) before after SCANF processing, which successfully eliminated cycle-slips (corrected hundreds of cycle-slips after the standard phase unwrapping) in this example. The TCWV retrievals are shown in Figure 2e, blue line (no noise filtering), and are compared with the ERA5 TCWV (green line, interpolated from the 0.25-degree grid data shown in Figure 2c). The black line shows the TCWV converted from $\widetilde{ZWD}$ as used in Eq. (7,8), which is interpolated from the VMF3 1-degree grid data. Figure 2f shows some consistency between GNSS-R retrievals and ERA5 models but does not seem to provide an effective assessment of accuracy. The TCWV retrievals below 3° are not expected to be accurate as the VMF3 mapping functions become less effective.

The second example is shown in Figure 3 using a set of Spire GNSS-R data recorded over another ocean area, with elevation angles from $\sim$5°$-$8°. Figure 3a shows the map of SLA, which is used in the GNSS-R geometry modeling in Eq (2,4). Figure 3b,c show the maps of ERA5 TCWV and Sentinel-3A OLCI IWV measurement, respectively. The

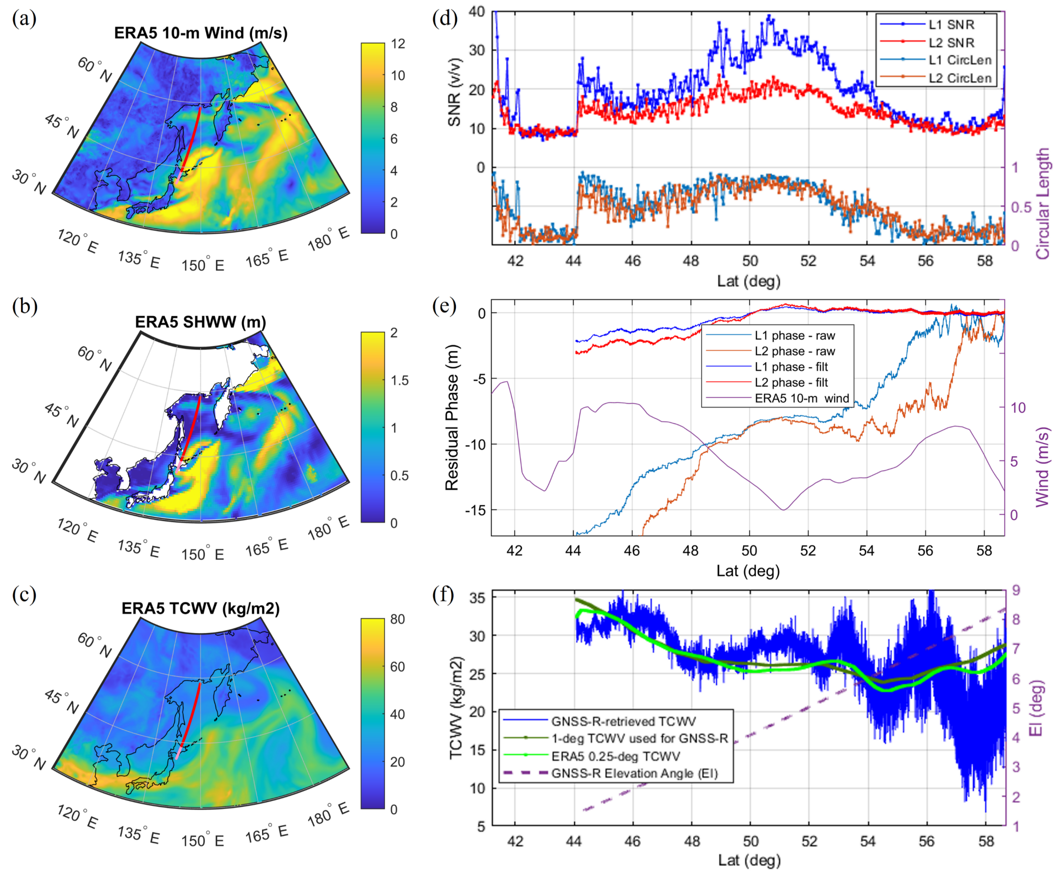

Figure 2: Processing, retrieval, and analysis of a grazing-angle GNSS-R example over the Sea of Okhotsk, using Spire data: spire_gnss-r_L1B_grzRfl_v07.10_2022-08-16 T17-09-21_FM104_G07_antFRO. (a)-(c) show maps of ERA5 10-m horizontal wind speed, significant height of wind wave (SHWW), and TCWV, respectively; (d) shows the GNSS-R measurement SNR and phase circular length (CircLen) from both L1 and L2 signals; (e) shows the GNSS-R L1 and L2 phase measurements before and after the SCANF reconstruction and the interpolated wind speed along the reflection track (corresponding to the y axis on the right); (f) shows the TCWV retrieved from GNSS-R and comparisons with interpolated TCWV from the 1-degree ZWD data (products used by VMF3 and used here as input to GNSS-R retrieval) and 0.25-degree ERA5 product, and the GNSS signal reflection elevation angle at the specular point (corresponding to the y axis on the right).

GNSS-R TCWV retrievals are compared against the ERA5 products and OLCI measurements in Figure 3d, where the GNSS-R retrievals show up to 20 $\text{kg}\cdot\text{m}^{-2}$ large fluctuations and is somewhat consistent with the OLCI measurements, while the ERA5 data (the brighter green line) is a lot flatter. An offset of a few $\text{kg}\cdot\text{m}^{-2}$ is also observed between the overall magnitudes of OLCI IWV measurements and the TCWV derived from VMF3 grid data, and it should affect the GNSS-R TCWV retrievals in both the mean magnitude and gradients.

The third example is shown in Figure 4 and is laid out in the same way as Figure 3. It confirms the feasibility and performance of the proposed approach with an additional case where the GNSS-R TCWV retrievals, using input information of a low resolution or low accuracy $\widetilde{ZWD}$ model, show consistent fluctuations with the OLCI IWV measurements and higher resolution ERA5 data products.

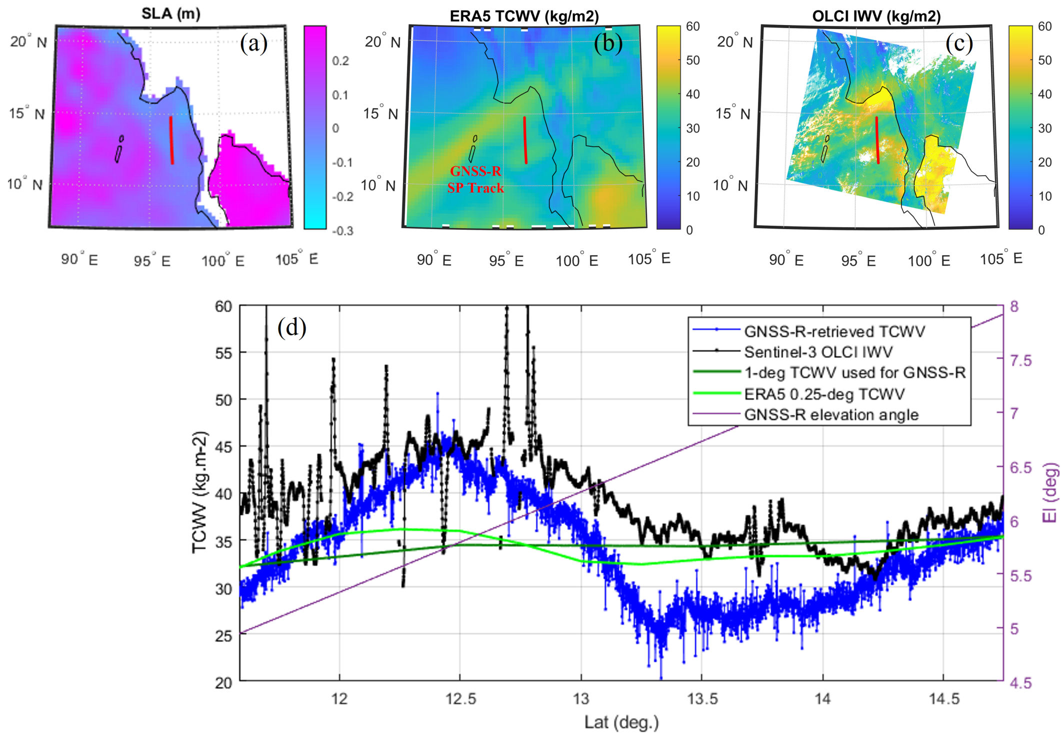

Figure 3: GNSS-R TCWV retrieval and validation case #1, over the Andaman Sea, using spire data: spire_gnss-r_L1B_grzRfl_v07.00_2022-01-17T03-45-56_FM100_G25_antFRO and Sentinel-3 data: S3B_OL_2_WFR_20220117T032845. (a)-(c) show maps of sea level anomaly (SLA), ERA5 TCWV, and Sentinel-3 OLCI IWV measurement, respectively; (d) shows the TCWV retrieved from GNSS-R and comparisons with interpolated TCWV from Sentinel-3 OLCI measurement, the 1-degree ZWD data (products used by VMF3 and used here as input to GNSS-R retrieval), and the 0.25-degree ERA5 product, and the GNSS signal reflection elevation angle at the specular point (corresponding to the y axis on the right).

5 Conclusion and Discussion

This paper studies a novel approach of using coherent reflection GNSS signals to sense the tropospheric delay and water vapor and presents the methodology and validation via case studies. This approach is proposed to sense the troposphere over the open ocean and ice, using GNSS signals reflected at very low elevation angles ($\sim 3° - 8°$), and the horizontal profiles of tropospheric delay and TCWV can be retrieved with centimeter-level high precision. The presented case studies using Spire grazing-angle GNSS-R data show promising TCWV retrievals as compared to Sentinel-3 OLCI measurements and ERA5 0.25-degree products.

The case study (in Figure 2) showed that GNSS signals can be coherently reflected over the ocean surface with ∼7-8 m/s wind speed (corresponding to 1-1.2 m significant wave height in that case) and at $\sim 7°$ elevation angle. Sea ice is also a good reflector for GNSS signals. Examples of GNSS-R TCWV retrievals over the Arctic sea ice have been presented in (Wang, 2023). A conservative estimation is presented in Roesler et al. (2021) and Wang and Morton (2021b) that ∼44% of the GPS signal reflections over sea ice is coherent, using spire data with elevation angles (somewhat evenly distributed) from $5° -$ $30°$. Given the fact that reflections tend to be more coherent at lower elevation angles,

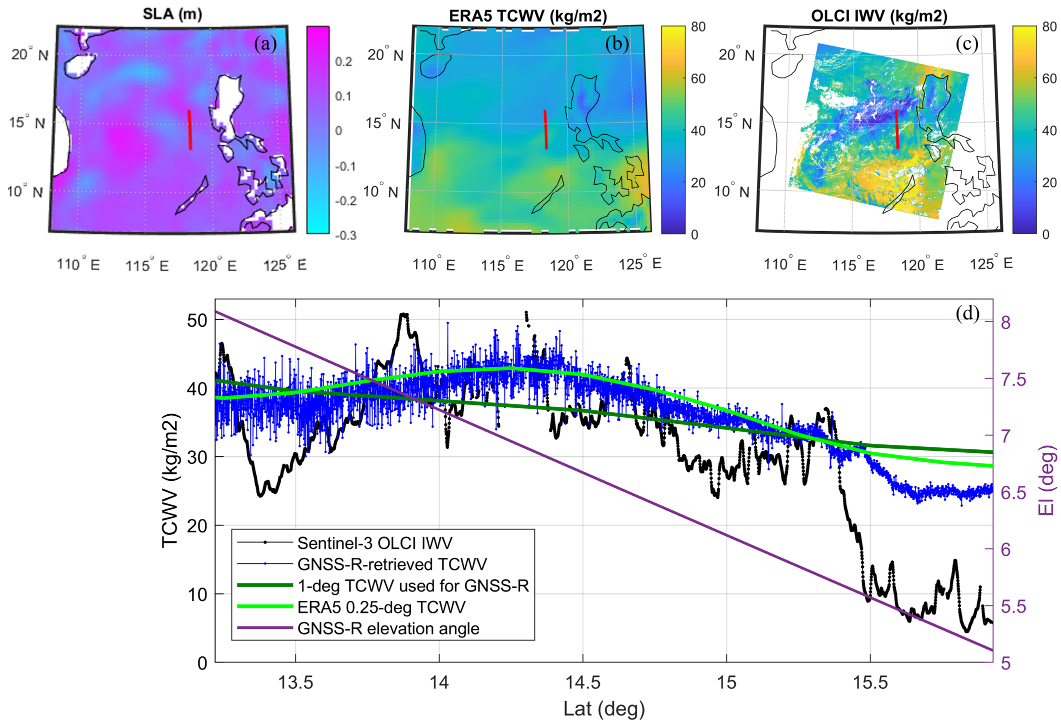

Figure 4: GNSS-R TCWV retrieval and validation case #2, over the South China Sea, using data: spire_gnss-r_L1B_grzRfl_v07.00_2022-03-05T02-13-10_FM122_G08_antBRO and Sentinel-3 data: S3A_OL_2_WFR_20220305T020830. (a)-(c) show maps of sea level anomaly (SLA), ERA5 TCWV, and Sentinel-3 OLCI IWV measurement, respectively; (d) shows the TCWV retrieved from GNSS-R and comparisons with interpolated TCWV from Sentinel-3 OLCI measurement, the 1-degree ZWD data (products used by VMF3 and used here as input to GNSS-R retrieval), and the 0.25-degree ERA5 product, and the GNSS signal reflection elevation angle at the specular point (corresponding to the y axis on the right).

this may indicate that the proposed approach can be applied to half of the ocean area, most sea ice, and some Antarctica and Greenland ice sheet areas. A more comprehensive characterization and analysis should be conducted in future work for GNSS signal reflected at $<8^\circ$ elevation angles to evaluate the applicable areas for the proposed approach.

The GNSS-R carrier phase only measures the relative slant tropospheric delay, due to the unknown phase ambiguities. The assumptions of stable ZHD and accurate mean magnitudes of ZWD model (e.g., from VMF3 or ERA5 grid data) may lead to elevation-dependent errors in the GNSS-R ZWD and TCWV retrievals, which therefore are not the ideal output of the tropospheric information inferred from GNSS-R measurements. Such errors should be characterized and quantified in future work, and a more effective way may be to incorporate or assimilate the lower-level GNSS-R slant tropospheric delay measurements $\hat{T_R}$ into meteorological models or systems.

Finally, the proposed approach is highly compatible with GNSS radio occultation in receiver hardware, onboard GNSS signal open loop processing, etc. The two approaches are complementary in geometry, i.e., vertical and horizontal profiles, and the signals reflected at $<3^\circ$ elevation angle should also be further exploited.

Open Research

The Spire grazing-angle GNSS-R data is accessed through the Smallsat Data explorer (available to U.S. Government funded researchers): https://www.earthdata.nasa.gov/esds/csda/smallsat-data-explorer. The Sentinel-3 data is available by ESA and can be accessed through the CREODIAS data explorer: https://explore.creodias.eu/. The ERA5 data is available from the Copernicus Climate Change Service (C3S) Climate Data Store (Hersbach et al., 2023). The SLA data is available from the Copernicus C3S Climate Data Store (Copernicus Climate Change Service, Climate Data Store, 2018). VMF3 data and tools are available from the VMF Data Server (re3data.org, 2021). The TPXO tide model data and tools are available from: https://www.tpxo.net/global. The DTU21 MSS data is available from the DTU Data (Andersen, 2022).

Acknowledgments

This study is partially supported by NASA grant 80NSSC23K1056. The Spire grazing-angle GNSS-R data utilized in this work was made available through the NASA Commercial Smallsat Data Acquisition (CSDA) Program.

References

Alshawaf, F., Fuhrmann, T., Knöpfler, A., Luo, X., Mayer, M., Hinz, S., & Heck, B. (2015). Accurate estimation of atmospheric water vapor using GNSS observations and surface meteorological data. *IEEE Transactions on Geoscience and Remote Sensing*, *53*(7), 3764–3771.

Andersen, O. B. (2022). DTU21 Mean Sea Surface. Technical University of Denmark. [dataset]. https://doi.org/10.11583/DTU.19383221.v1. *(Accessed on 2023-10-30)*.

Andersen, O. B., Rose, S. K., Abulaitijiang, A., Zhang, S., & Fleury, S. (2023). The dtu21 global mean sea surface and first evaluation. *Earth System Science Data Discussions*, *2023*, 1–19.

Anthes, R. (2011). Exploring Earth's atmosphere with radio occultation: Contributions to weather, climate and space weather. *Atmospheric Measurement Techniques*, *4*(6), 1077–1103.

Ault, T. R. (2020). On the essentials of drought in a changing climate. *Science*, *368*(6488), 256–260.

Bengtsson, L., & Hodges, K. I. (2005). On the impact of humidity observations in numerical weather prediction. *Tellus A: Dynamic Meteorology and Oceanography*, *57*(5), 701–708.

Bevis, M., Businger, S., Chiswell, S., Herring, T. A., Anthes, R. A., Rocken, C., & Ware, R. H. (1994). GPS meteorology: Mapping zenith wet delays onto precipitable water. *Journal of Applied Meteorology (1988-2005)*, 379–386.

Bevis, M., Businger, S., Herring, T. A., Rocken, C., Anthes, R. A., & Ware, R. H. (1992). GPS meteorology: Remote sensing of atmospheric water vapor using the global positioning system. *Journal of Geophysical Research: Atmospheres*, *97*(D14), 15787–15801.

Bojinski, S., Verstraete, M., Peterson, T. C., Richter, C., Simmons, A., & Zemp, M. (2014). The concept of essential climate variables in support of climate research, applications, and policy. *Bulletin of the American Meteorological Society*, *95*(9), 1431–1443.

Cardellach, E., Li, W., Rius, A., Semmling, M., Wickert, J., Zus, F., ... Buontempo, C. (2019). First precise spaceborne sea surface altimetry with GNSS reflected signals. *IEEE Journal of Selected Topics in Applied Earth Observations and Remote Sensing*, *13*, 102–112.

Copernicus Climate Change Service, Climate Data Store. (2018). Sea level gridded data from satellite observations for the global ocean from 1993 to present.

copernicus climate change service (c3s) climate data store (cds). [dataset]. *DOI: 10.24381/cds.4c328c78. (Accessed on 2023-10-30).*

Egbert, G. D., & Erofeeva, S. Y. (2002). Efficient inverse modeling of barotropic ocean tides. *Journal of Atmospheric and Oceanic Technology*, *19*(2), 183–204.

Elgered, G., Davis, J., Herring, T., & Shapiro, I. (1991). Geodesy by radio interferometry: Water vapor radiometry for estimation of the wet delay. *Journal of geophysical research: solid earth*, *96*(B4), 6541–6555.

Hersbach, H., Bell, B., Berrisford, P., Biavati, G., Horányi, A., Muñoz Sabater, J., ... others (2023). Era5 hourly data on single levels from 1940 to present. [dataset]. *Copernicus climate change service (c3s) climate data store (cds), DOI: 10.24381/cds.adbb2d47. (Accessed on 2023-10-30).*

Ismail, S., & Browell, E. V. (1989). Airborne and spaceborne lidar measurements of water vapor profiles: a sensitivity analysis. *Applied Optics*, *28*(17), 3603–3615.

Jales, P., Esterhuizen, S., Masters, D., Nguyen, V., Correig, O. N., Yuasa, T., & Cartwright, J. (2020). The new Spire GNSS-R satellite missions and products. In *Image and signal processing for remote sensing xxvi* (Vol. 11533, p. 1153316).

Kuo, Y.-H., Sokolovskiy, S. V., Anthes, R. A., & Vandenberghe, F. (2000). Assimilation of GPS radio occultation data for numerical weather prediction. *Terrestrial Atmospheric and Oceanic Sciences*, *11*(1), 157–186.

Landskron, D., & Böhm, J. (2018). VMF3/GPT3: refined discrete and empirical troposphere mapping functions. *Journal of geodesy*, *92*, 349–360.

Li, W., Cardellach, E., Fabra, F., Ribo, S., & Rius, A. (2018). Lake level and surface topography measured with spaceborne GNSS-reflectometry from CYGNSS mission: Example for the lake Qinghai. *Geophysical Research Letters*, *45*(24), 13–332.

Li, W., Cardellach, E., Fabra, F., Rius, A., Ribó, S., & Martín-Neira, M. (2017). First spaceborne phase altimetry over sea ice using TechDemoSat-1 GNSS-R signals. *Geophysical Research Letters*, *44*(16), 8369–8376.

Li, Z., Muller, J.-P., & Cross, P. (2003). Comparison of precipitable water vapor derived from radiosonde, GPS, and Moderate-Resolution Imaging Spectroradiometer measurements. *Journal of Geophysical Research: Atmospheres*, *108*(D20).

Loria, E., Russo, I. M., Wang, Y., Giangregorio, G., Galdi, C., Di Bisceglie, M., ... others (2023). Comparison of GNSS-R Coherent Reflection Detection Algorithms Using Simulated and Measured CYGNSS Data. *IEEE Transactions on Geoscience and Remote Sensing*.

Masson-Delmotte, V., Zhai, P., Pirani, A., Connors, S. L., Péan, C., Berger, S., ... others (2021). Climate change 2021: the physical science basis. *Contribution of working group I to the sixth assessment report of the intergovernmental panel on climate change*, *2*.

Miloshevich, L. M., Vömel, H., Whiteman, D. N., Lesht, B. M., Schmidlin, F., & Russo, F. (2006). Absolute accuracy of water vapor measurements from six operational radiosonde types launched during AWEX-G and implications for AIRS validation. *Journal of Geophysical Research: Atmospheres*, *111*(D9).

Nguyen, V. A., Nogués-Correig, O., Yuasa, T., Masters, D., & Irisov, V. (2020). Initial GNSS phase altimetry measurements from the spire satellite constellation. *Geophysical Research Letters*, *47*(15), e2020GL088308.

Niell, A., Coster, A., Solheim, F., Mendes, V., Toor, P., Langley, R., & Upham, C. (2001). Comparison of measurements of atmospheric wet delay by radiosonde, water vapor radiometer, GPS, and VLBI. *Journal of Atmospheric and Oceanic Technology*, *18*(6), 830–850.

re3data.org. (2021). VMF Data Server; editing status 2021-08-24; re3data.org - Registry of Research Data Repositories. [dataset]. *http://doi.org/10.17616/R3RD2H. last accessed: 2023-10-30*.

Roesler, C. J., Morton, Y. J., Wang, Y., & Nerem, R. S. (2021). Coherent GNSS-reflections characterization over ocean and sea ice based on spire global CubeSat data. *IEEE Transactions on Geoscience and Remote Sensing*, *60*, 1–18.

Schneider, T., O'Gorman, P. A., & Levine, X. J. (2010). Water vapor and the dynamics of climate changes. *Reviews of Geophysics*, *48*(3).

Sherwood, S., Roca, R., Weckwerth, T., & Andronova, N. (2010). Tropospheric water vapor, convection, and climate. *Reviews of Geophysics*, *48*(2).

Steiner, A., & Kirchengast, G. (2005). Error analysis for GNSS radio occultation data based on ensembles of profiles from end-to-end simulations. *Journal of Geophysical Research: Atmospheres*, *110*(D15).

Turato, B., Reale, O., & Siccardi, F. (2004). Water vapor sources of the October 2000 Piedmont flood. *Journal of Hydrometeorology*, *5*(4), 693–712.

Wang, Y. (2023). Grazing-angle GNSS-R for the Determination of Tropospheric Delay and Water Vapor Content. In *Proceedings of the 36th International Technical Meeting of the Satellite Division of The Institute of Navigation (ION GNSS+ 2023)* (pp. 3227–3232).

Wang, Y., Breitsch, B., & Morton, Y. T. J. (2020). A state-based method to simultaneously reduce cycle slips and noise in coherent GNSS-R phase measurements from open-loop tracking. *IEEE Transactions on Geoscience and Remote Sensing*, *59*(10), 8873–8884.

Wang, Y., & Morton, Y. J. (2021a). Evaluation of GNSS-R retrieved sea ice surface height using ICESat-2 ice freeboard measurements. In *2021 IEEE International Geoscience and Remote Sensing Symposium IGARSS* (pp. 7803–7806).

Wang, Y., & Morton, Y. J. (2021b). Ionospheric total electron content and disturbance observations from space-borne coherent GNSS-R measurements. *IEEE Transactions on Geoscience and Remote Sensing*, *60*, 1–13.

Wang, Y., & Morton, Y. J. (2021c). River slope observation from spaceborne GNSS-R carrier phase measurements: a case study. *IEEE Geoscience and Remote Sensing Letters*, *19*, 1–5.

Yuan, P., Blewitt, G., Kreemer, C., Hammond, W. C., Argus, D., Yin, X., . . . others (2023). An enhanced integrated water vapour dataset from more than 10 000 global ground-based GPS stations in 2020. *Earth System Science Data*, *15*(2), 723–743.

Figure 1.

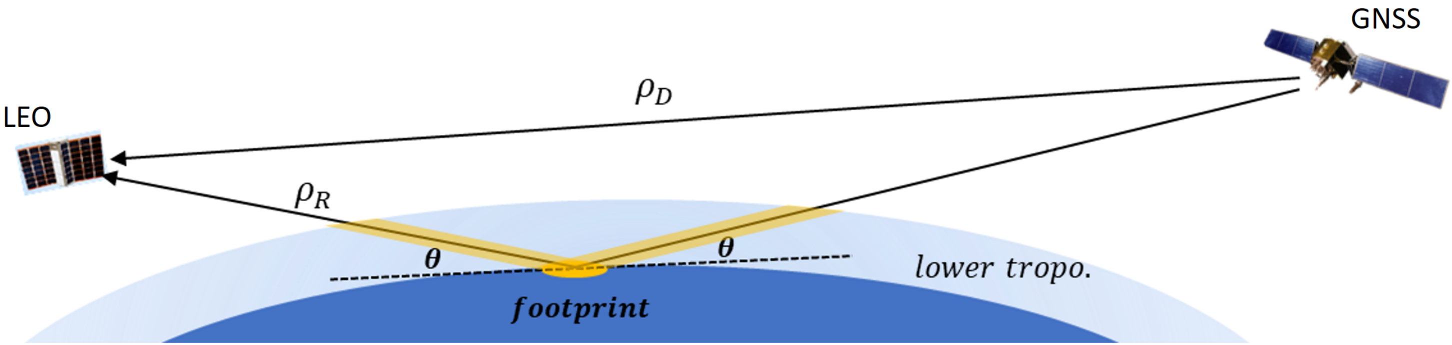

GNSS
LEO
ρ_D
ρ_R
θ
θ
lower tropo.
footprint

(a)

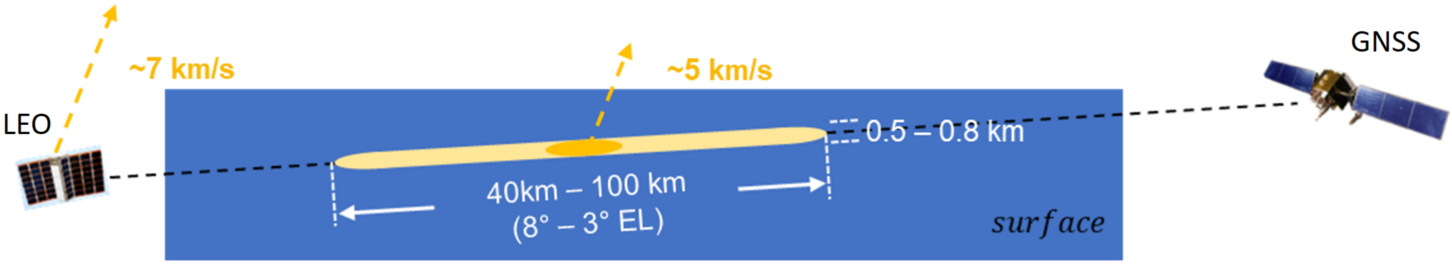

~7 km/s
~5 km/s
GNSS
LEO
0.5 – 0.8 km
40km – 100 km
(8° – 3° EL)
surface

(b)

Figure 2.

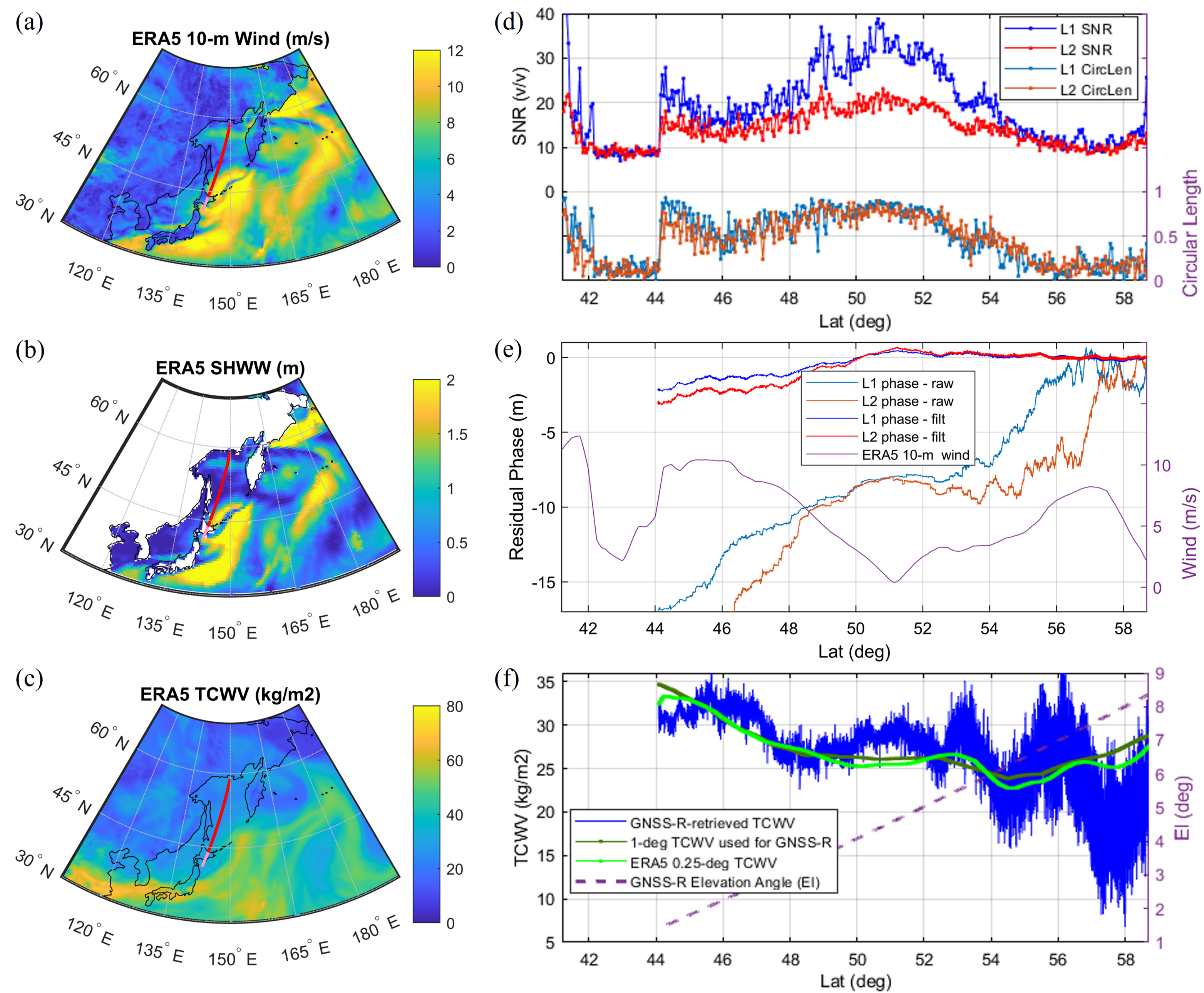
(a)
ERA5 10-m Wind (m/s)
(b)
ERA5 SHWW (m)
(c)
ERA5 TCWV (kg/m2)
60° N
45° N
30° N
120° E
135° E
150° E
165° E
180° E
(d)
SNR (v/v)
Circular Length
L1 SNR
L2 SNR
L1 CircLen
L2 CircLen
Lat (deg)
(e)
Residual Phase (m)
Wind (m/s)
L1 phase - raw
L2 phase - raw
L1 phase - filt
L2 phase - filt
ERA5 10-m wind
Lat (deg)
(f)
TCWV (kg/m2)
El (deg)
GNSS-R-retrieved TCWV
1-deg TCWV used for GNSS-R
ERA5 0.25-deg TCWV
GNSS-R Elevation Angle (El)
Lat (deg)

Figure 3.

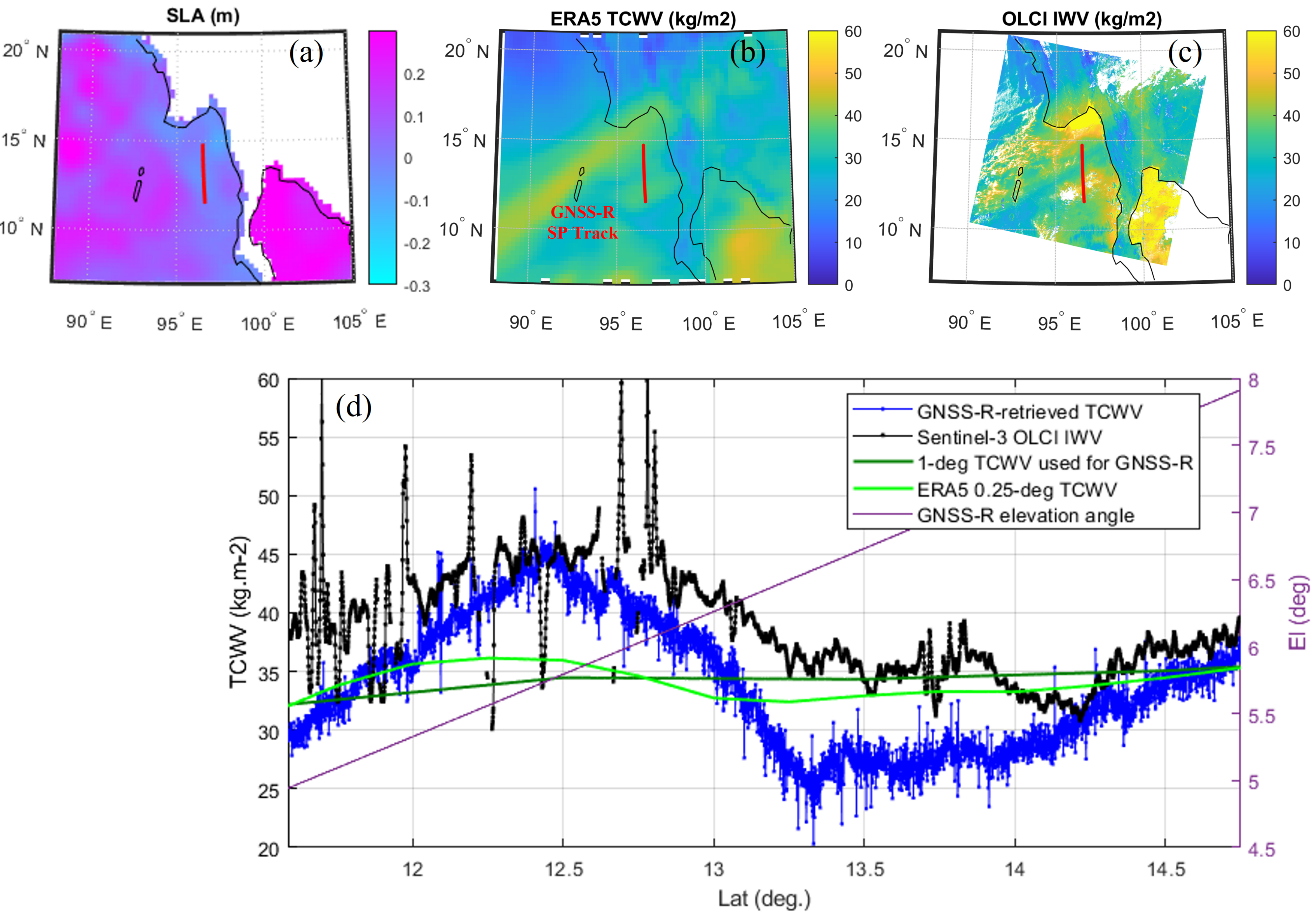

SLA (m)
(a)
ERA5 TCWV (kg/m2)
(b)
GNSS-R
SP Track
OLCI IWV (kg/m2)
(c)
20° N
15° N
10° N
90° E
95° E
100° E
105° E
(d)
GNSS-R-retrieved TCWV
Sentinel-3 OLCI IWV
1-deg TCWV used for GNSS-R
ERA5 0.25-deg TCWV
GNSS-R elevation angle
TCWV (kg.m-2)
El (deg)
Lat (deg.)

Figure 4.

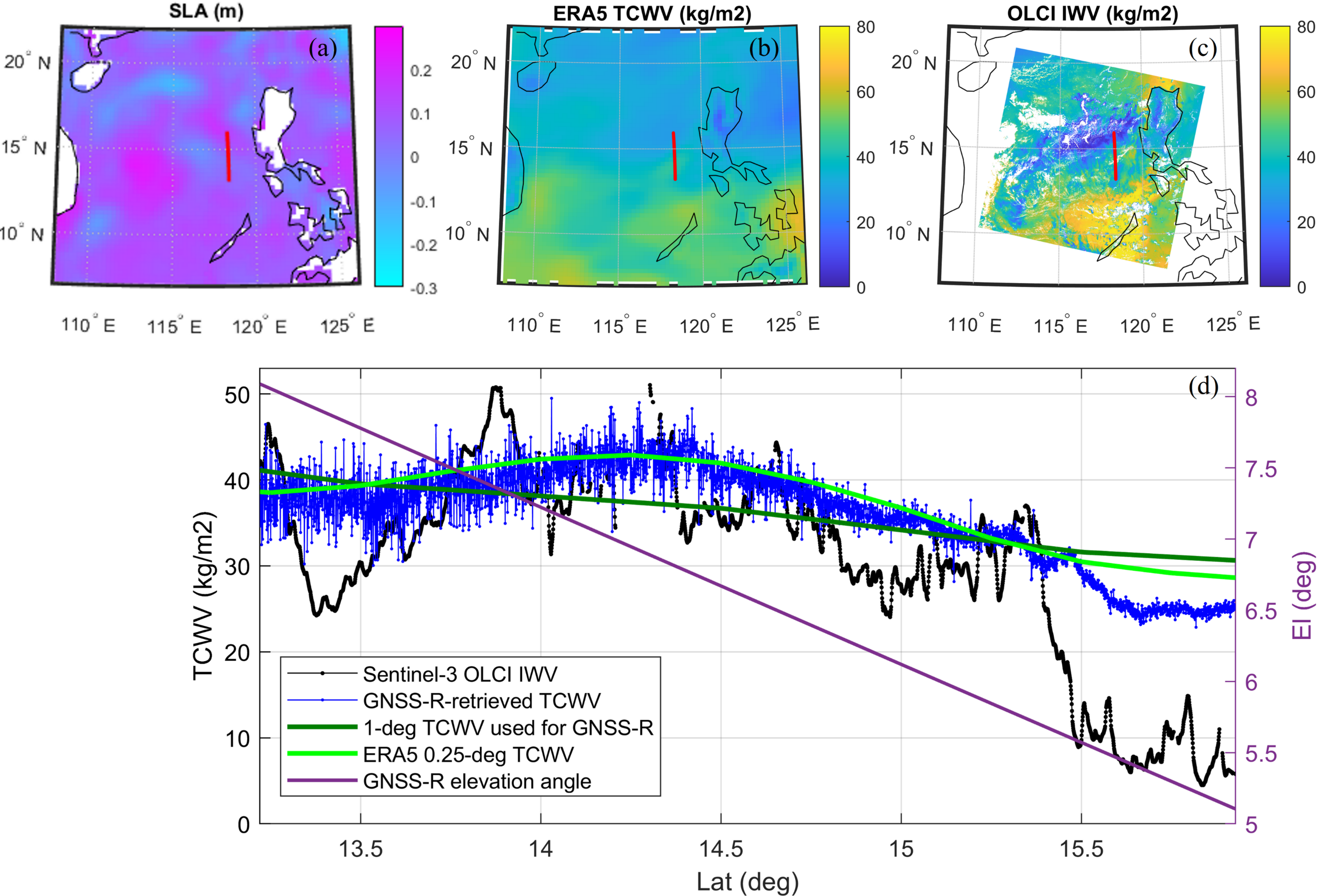
SLA (m)
(a)
ERA5 TCWV (kg/m2)
(b)
OLCI IWV (kg/m2)
(c)
20° N
15° N
10° N
110° E
115° E
120° E
125° E
(d)
TCWV (kg/m2)
El (deg)
Lat (deg)
Sentinel-3 OLCI IWV
GNSS-R-retrieved TCWV
1-deg TCWV used for GNSS-R
ERA5 0.25-deg TCWV
GNSS-R elevation angle